https://dx.doi.org/10.1016/j.ijmecsci.2023.108669

Customizable multiband second-order sonic topological insulators via inverse design

Yafeng Chen[1†], Xueyun Wen[2†], Zhongming Gu[2*], Jie Zhu[2#], and Zhongqing Su[1§]

[1] *Department of Mechanical Engineering, The Hong Kong Polytechnic University, Kowloon, Hong Kong SAR, China*

[2]*Institute of Acoustics, School of Physics Science and Engineering, Tongji University, 200092, Shanghai, China*

Abstract

The second-order sonic topological insulators (SSTIs) with topologically protected corner states offer promising opportunities for developing novel acoustic devices. However, most of the current SSTIs are designed via trial-and-error and are only able to host the second-order topological phases within a single bandgap, leaving the topic of second-order topological phases within multiple bandgaps rarely studied. Here, we exploit a topology optimization method to customize and optimize multiband SSTIs. To begin with, we create multiple dual-band SSTIs with customizable dual bandgaps for hosting dual-band corner states. On that basis, a three-band SSTI with three bandgaps is constructed for hosting three-band corner states. Experimental validation is performed to prove the existence of the three-band corner states. This study ushers in a route for customizing high-performance multiband SSTIs, and the designed multiband SSTIs have potential for designing robust multiband acoustic devices.

Keywords: *second-order topological insulators; corner states; multiband topological phases; sonic crystals.*

[†]These authors contributed equally to this work.
[*] zhmgu@tongji.edu.cn
[#] jiezhu@tongji.edu.cn
[§]zhongqing.su@polyu.edu.hk

1. Introduction

Sonic topological insulators (STIs), featuring topologically protected boundary states that are resilient against impurities, provide a route for manipulating acoustic waves robustly, offering opportunities for developing novel acoustic devices [1-8]. To date, by mimicking topological insulators (TIs) in electric and photonic systems [9], various versions of STIs have been realized, such as quantum Hall effects-based STIs [10], quantum spin Hall effect (QSHE)-based STIs [11], quantum valley Hall effect (QVHE)-based STIs [12, 13], Floquet STIs [14], and so on. These STIs all follow the conventional bulk-boundary correspondence and host topologically protected gapless edge states. Recently, a new version of STI, the higher-order STI (HSTI), has been realized, which goes beyond conventional bulk-boundary correspondence and supports hierarchical boundary states [15-20]. For example, in two-dimensional systems, the HSTI, also called second-order STI (SSTI), supports gapped edge states within the bulk gap and corner states within the edge gap. For constructing SSTIs, crystalline symmetry plays a vital role. Hitherto, multiple kinds of dipolar SSTIs based on different lattices with various symmetries have been proposed, e.g., square lattices with glide and C_{4v} symmetries [16, 21], hexagonal lattices with C_{6v} and C_3 symmetries [22, 23], kagome lattice with C_3 symmetry [15], etc. Besides, diverse quadrupolar SSTIs [17, 24] and sonic higher-order Weyl semimetal [25] have also been created. However, most of the current SSTIs only support topological corner states within only one bandgap, restricting their applications in multiband communications, filters, waveguides, information processions and so forth. Moreover, in some applications, e.g. nonlinear frequency conversion, it is also desirable to design multiband topological modes [26]. Recently, Zhang et al. [24] created the sonic crystal (SC) with two bandgaps hosting dipolar and quadrupolar topological phases, respectively. However, only the quadrupolar corner states are demonstrated. Fan et al. designed a perforated metaplate hosting local-resonance-induced dual-band topological

corner states of elastic flexural waves [27]. However, it still needs to explore the SSTIs hosting multiband dipolar corner states, which are yet unsettled.

On the other hand, current SSTIs are mainly created via trial-and-error, thus their capabilities may be severely restricted. For example, the size of bulk bandgaps is small, thereby resulting in that the topological edge and corner states are not tightly localized. As the performance of SSTIs rests with the configurations of trivial and nontrivial unit cells (UCs), it is preferable to use the inverse design approach to design trivial and nontrivial UCs for constructing SSTIs [28]. Fairly recently, the inverse design method has been exploited to create QSHE-based STIs and photonic TIs with wide edge states [29-34], QVHE-based phononic and photonic TIs with wide edge states [35-37], second-order phononic and photonic TIs with tightly localized corner states [38-44], and valley-selective SSTIs [45], indicating its great abilities in constructing TIs with high performance. However, designing SSTIs hosting multiband corner states via inverse design still remains unexplored.

Here, we utilize the topology optimization, an inverse design method, for customizing multiband SSTIs. We first create multiple dual-band SSTIs with customizable dual bandgaps for hosting corner states. On that basis, a three-band SSTI hosting corner states within three bandgaps is constructed. Thereafter, we fabricate the three-band SSTI via 3D printing and conduct an experiment to verify the three-band corner states. The remaining paper is arranged as: Section 2 describes the developed inverse design framework; Section 3 presents the optimized dual-band and three-band SSTIs, and the relevant experimental results; Section 4 gives the summary.

2. Inverse design framework

Here, we focus on the dipolar SSTIs in C_{4v}-symmetric lattices. Our previous studies on second-order photonic topological insulators show that dipolar topological phases in C_{4v}-symmetric square lattices can be achieved within the odd-order bandgap, that is, the odd-order bandgap can be used as precursors for constructing second-order dipolar topological phases [46, 47] in C_{4v}-symmetric square lattices. As in two-dimensional systems, acoustic waves and electromagnetic waves are all scalar waves with one degree of freedom, many topology properties of photonic crystals can be also transplanted into SCs. We anticipate that second-order dipolar topological phases can be also achieved within the odd-order bandgap of SCs. Therefore, the inverse design framework is formulated to design multiple odd-order bandgaps to further realize multiband second-order dipolar topological phases. In this section, we will introduce the inverse design framework, including the finite element analysis of SCs, the optimization objective function, the optimization constraint function, the inverse design formulation, and the numerical implementation of the optimization.

2.1. Finite element analysis of SCs

Without the internal sources, the acoustic waves propagating in SCs are governed by [48]

$$-\nabla\cdot\left(\frac{1}{\rho(\mathbf{r})}\nabla p(\mathbf{r},\mathbf{k})\right)+\frac{1}{B(\mathbf{r})}\frac{\partial^2 p(\mathbf{r},\mathbf{k})}{\partial t^2}=0 \tag{1}$$

in which $p(\mathbf{r},\mathbf{k})$ denotes the acoustic pressure field; $\mathbf{r}(x,y)$ represents the position vector; ρ and B are the density and bulk modulus, respectively; $\mathbf{k}=(k_x,k_y)$ represents the Bloch wave vector. Because of the SCs' periodicity, $\rho(\mathbf{r})=\rho(\mathbf{r}+\mathbf{R})$ and $B(\mathbf{r})=B(\mathbf{r}+\mathbf{R})$, where $\mathbf{R}$ denotes the lattice translation vector. Based on the Floquet-Bloch theorem [49], we can formulate the pressure field as

$$p(\mathbf{r},\mathbf{k})=p_{\mathbf{k}}(\mathbf{r})e^{i(\omega t+\mathbf{k}\cdot\mathbf{r})} \tag{2}$$

Taking Eq. (2) into Eq. (1) and using the finite element method, Eq. (1) can be expressed by

$$\left(\mathbf{K}-\omega^2\mathbf{M}\right)\mathbf{p}=0 \tag{3}$$

where ω is the eigenvalue of angular frequency; $\mathbf{p}$ denotes the eigenvector of acoustic pressure field; $\mathbf{K}$ is the global stiffness matrix; $\mathbf{M}$ is the global mass matrix. Note that the 4-node plane strain element is adopted and the shape function $\mathbf{N}$ is expressed by [N1, N2, N3, N4]. We can get the band diagram by sweeping the wave vector $\mathbf{k}$ along the boundary of the first Brillouin zone, as sketched in Fig. 1, and solving Eq. (3).

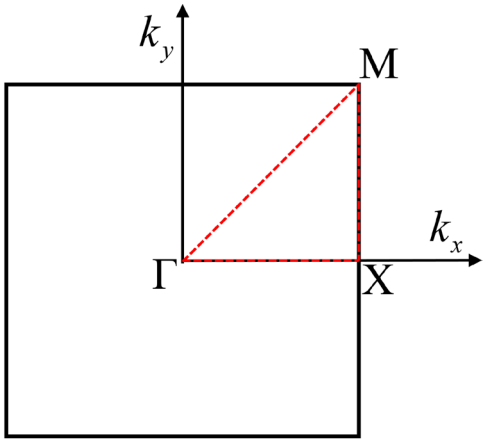

Fig. 1. Schematic of the boundary of the first Brillouin zone.

2.2. Optimization objective function

Hence, we adopt the inverse design method to design the C_{4v}-symmetric SCs with multiple odd-order bandgaps, which are further exploited to design multiband SSTIs. For designing SCs, the relative width of the specific n-order bandgap, g_n, is selected as the optimization objective, expressed byg

$$g_n = 2\frac{\min\limits_{i=1,2,\cdots n_k}\omega_{n+1}\left(\mathbf{k}_i\right)-\max\limits_{i=1,2,\cdots n_k}\omega_n\left(\mathbf{k}_i\right)}{\min\limits_{i=1,2,\cdots n_k}\omega_{n+1}\left(\mathbf{k}_i\right)+\max\limits_{i=1,2,\cdots n_k}\omega_n\left(\mathbf{k}_i\right)} \tag{4}$$

where n_k denotes the total number of wave vectors considered. To avoid numerical instabilities, we used the strategy proposed in refs. [50, 51] to modify the objective function.

First, two bounds, $C_1 = 0.9\max\omega_n(\mathbf{k}_i)$ and $C_2 = 1.1\min\omega_{n+1}(\mathbf{k}_i)$ are introduced. Then, all points with $\omega(\mathbf{k}_i) \in \left[C_1, \max\omega_n(\mathbf{k}_i)\right]$ are taken into account for calculating the lower boundary of the band gap. In the meantime, all points with $\omega(\mathbf{k}_i) \in \left[\min\omega_{n+1}(\mathbf{k}_i), C_2\right]$ are taken into account for calculating the upper boundary of the band gap. As such, we can modify the objective function as

$$\tilde{g}_n = 2\frac{\sum_{i=1}^{n_k}\sum_{j=n+1}^{\infty} w_{ij}\omega_j(\mathbf{k}_i) - \sum_{i=1}^{n_k}\sum_{j=1}^{n} \hat{w}_{ij}\omega_j(\mathbf{k}_i)}{\sum_{i=1}^{n_k}\sum_{j=n+1}^{\infty} w_{ij}\omega_j(\mathbf{k}_i) + \sum_{i=1}^{n_k}\sum_{j=1}^{n} \hat{w}_{ij}\omega_j(\mathbf{k}_i)} \tag{5}$$

where w_{ij} and $\hat{w}_{ij}$ denote weight factors, expressed by

$$w_{ij} = \frac{A_{ij}}{\sum_{i=1}^{n_k}\sum_{n+1}^{\infty} A_{ij}} \tag{6a}$$

$$\hat{w}_{ij} = \frac{\hat{A}_{ij}}{\sum_{i=1}^{n_k}\sum_{1}^{n} \hat{A}_{ij}} \tag{6b}$$

in which A_{ij} and $\hat{A}_{ij}$ are defined as

$$A_{ij} = \begin{cases} C_2 - \omega_j(\mathbf{k}_i) & \text{when } \omega_j(\mathbf{k}_i) < C_2 \\ 0 & \text{otherwise} \end{cases} \tag{7a}$$

$$\hat{A}_{ij} = \begin{cases} \omega_j(\mathbf{k}_i) - C_1 & \text{when } \omega_j(\mathbf{k}_i) > C_1 \\ 0 & \text{otherwise} \end{cases} \tag{7b}$$

As a result, $\sum_{i=1}^{n_k}\sum_{j=n+1}^{\infty} w_{ij} = 1$ and $\sum_{i=1}^{n_k}\sum_{j=1}^{n} \hat{w}_{ij} = 1$.

For optimizing the multiple bandgaps, we first use the $\left\{f_1, f_2, \cdots f_{N_d}\right\}$ to record the relative size of multiple bandgaps $\left\{\tilde{g}_{n_1}, \tilde{g}_{n_2}, \cdots \tilde{g}_{n_{N_d}}\right\}$, where N_d denotes the number of objective

bandgaps. Then, the optimization objective is formulated as [52]

$$f = \min\left\{f_1, f_2, \cdots f_{N_d}\right\} \approx -\frac{1}{\gamma}\ln\left\{\sum_{j=1}^{N}\exp\left(-\gamma f_j\right)\right\} + \frac{1}{\gamma}\ln\left(N\right) \tag{8}$$

where γ is the aggregation parameter of the Kreisselmeire-Steinhauser function [52] and is selected to be 20.

In the optimization, we restrict the unit cell with C_{4v} symmetry and discretize it into 60×60 elements. We assign each element a design variable x_e, where $x_e = 1$ means the element is air and $x_e = 0$ denotes the element is resin epoxy. For the element with intermediate value, we adopt the inverse linear material interpolation to represent its density and bulk modulus [29, 53]:

$$\frac{1}{\rho(x_e)} = \left(1 - x_e\right)\frac{1}{\rho_1} + x_e\frac{1}{\rho_2} \tag{9}$$

$$\frac{1}{B(x_e)} = \left(1 - x_e\right)\frac{1}{B_1} + x_e\frac{1}{B_2} \tag{10}$$

where $\rho_1 = 1180\text{kg}/\text{m}^3$ and $\rho_2 = 1.2041\text{kg}/\text{m}^3$ denote the densities of resin epoxy and air, respectively; $B_1 = 7.58\text{GPa}$ and $B_2 = 1.42\times10^{-5}\text{GPa}$ mean the bulk modulus of resin epoxy and air, respectively.

2.3. Optimization constraint function

In SCs, the air domain should be connected into a block. However, if we solely maximize the bandgap without any connectivity constraints, the air may form some isolated domains, which can cause numerical errors during the optimization. To solve this problem, we impose a constraint function to ensure the air domains are fully connected in the optimized SCs. We assume a new periodic material made of the unit cell with each element having the same design variable as the original unit cell for optimizing the bandgap. However, in the new

material, $x_e = 1$ represents the element is full of hard material with elastic modulus of E_0 whereas $x_e = 0$ means the element is full of soft material with elastic modulus of $10^{-3} E_0$; the Poisson ratio of both the hard and soft materials is selected to be 0.3. For the element with an intermediate variable, we adopt the solid isotropic material penalization (SIMP) model [54] to represent its elastic modulus:

$$E\left(x_e\right) = 10^{-3} E_0 \left(1 - x_e^3\right) + E_0 x_e^3 \tag{11}$$

The effective bulk modulus κ^H of the new assumed periodic material is selected as the constraint function, which is constrained to be larger than a specific value, κ^*, during the optimization to ensure that all elements with $x_e = 1$ are fully connected. According to the homogenization theory [54, 55], the effective elasticity matrix of the new material is

$$E_{lm}^H = \frac{1}{|Y|} \int_\Omega \left(\left\{ \varepsilon_0^l \right\} - \left\{ \varepsilon^l \right\} \right)^T \left[E \right] \left(\left\{ \varepsilon_0^m \right\} - \left\{ \varepsilon^m \right\} \right) d\Omega \tag{12}$$

where E_{lm}^H denotes the homogenized elasticity matrix of the new material and, in two dimension systems, l,m = 1,2,3; $\left[E\right]$ represents the elasticity matrix of the constituent at a given position within the domain, denoted by Ω, of the unit cell; $|Y|$ is the unit cell's area; $\left\{ \varepsilon_0^{l,m} \right\}$ means the three linear independent test strain fields, and $\left\{ \varepsilon_0^1 \right\} = \left\{1,0,0\right\}$, $\left\{ \varepsilon_0^2 \right\} = \left\{0,1,0\right\}$, $\left\{ \varepsilon_0^3 \right\} = \left\{0,0,1\right\}$ in two dimension systems. The resulting strain fields $\left\{ \varepsilon^{l,m} \right\}$ are the solutions to standard finite element problems subjected to the test strain. We can calculate the homogenized bulk modulus κ^H according to the components of the effective elasticity matrix:

$$\kappa^H = \frac{1}{4} \left(E_{11}^H + E_{12}^H + E_{21}^H + E_{22}^H \right) \tag{13}$$

For a two-phase periodic material, we can estimate the maximum bulk modulus based on the

Hashin-Shtrikman (HS) bounds [56]. With a specific volume fraction of hard material, V_f^2, the maximum of the bulk modulus is

$$\kappa_{\max} = \frac{V_f^2 G_2}{\left(1 - V_f^2\right)\kappa_2 + G_2} \tag{14}$$

where κ_2 and G_2 denote the hard materials' static bulk modulus and shear modulus, respectively. Herein we define the constraint function as $\kappa^H \geq \kappa^* = \beta\kappa_{\max}$.

2.4. Inverse design formulation

According to the objective and constraint functions, we can formulate the optimization problem as

$$\begin{cases} \max: \ f\left(x_e\right) \\ \text{s . t.}: \kappa^H \geq \kappa^* = \beta\kappa_{\max} \\ \qquad V_f^2 = V_f^* \\ \qquad x_e = 0 \text{ or } 1; e = 1, 2, \cdots, n_e \end{cases} \tag{15}$$

in which n_e denotes the number of elements, V_f^* is the objective volume fraction of air. We will use the bi-directional evolutionary structure optimization (BESO) method [57] to solve Eq. (15), thus the objective and constraint functions' sensitivities should be derived. According to Eqs. (5) and (8), the objective function's sensitivity, $\frac{\partial f}{\partial x_e}$, can be derived upon getting $\frac{\partial \omega_n\left(\mathbf{k}_i\right)}{\partial x_e}$, which can be calculated by differentiating both sides of Eq. (3):

$$\frac{\partial \omega_n\left(\mathbf{k}_i\right)}{\partial x_e} = \frac{1}{2\omega_n}\mathbf{p}^T\left(\frac{\partial \mathbf{K}}{\partial x_e} - \omega_n^2\left(\mathbf{k}_i\right)\frac{\partial \mathbf{M}}{\partial x_e}\right)\mathbf{p} \tag{16}$$

Based on Eq. (13), the constraint function's sensitivity is

$$\frac{\partial \kappa^H}{\partial x_e} = \frac{1}{4}\left(\frac{\partial E_{11}^H}{\partial x_e} + \frac{\partial E_{12}^H}{\partial x_e} + \frac{\partial E_{21}^H}{\partial x_e} + \frac{\partial E_{22}^H}{\partial x_e}\right) \tag{17}$$

We can calculate the derivative of the homogenized elasticity matrix, $\frac{\partial E_{lm}^H}{\partial x_e}$, using the adjoint variable method [58]:

$$\frac{\partial E_{lm}^H}{\partial x_e} = \frac{1}{|Y|}\int_\Omega \left(\left\{\varepsilon_0^l\right\} - \left\{\varepsilon^l\right\}\right)^T \frac{\partial E_{lm}}{\partial x_e}\left(\left\{\varepsilon_0^m\right\} - \left\{\varepsilon^m\right\}\right) d\Omega \tag{18}$$

Plugging Eq. (11) into Eq. (18), the derivative of the homogenized elasticity matrix is

$$\frac{\partial E_{lm}^H}{\partial x_e} = \frac{p x_e^2}{|Y|}\int_\Omega \left(\left\{\varepsilon_0^l\right\} - \left\{\varepsilon^l\right\}\right)^T \left(E_{lm}^2 - E_{lm}^1\right)\left(\left\{\varepsilon_0^m\right\} - \left\{\varepsilon^m\right\}\right) d\Omega \tag{19}$$

where E_{lm}^1 and E_{lm}^2 represent the elasticity matrix of soft material and hard material, respectively.

2.5. Numerical implementation

As seen in Eq. (15), the optimization problem has two constraints, that is, a volume constraint and a bulk modulus constraint. Generally, in BESO [57], the volume constraint is automatically implemented, whereas the extra constraint is imposed by adding it to the objective function by introducing a Lagrangian multiplier, λ [53, 59, 60], expressed by

$$f^* = f + \lambda\left(\kappa^H - \kappa^*\right) \tag{20}$$

Therefore, the above modified objective function's sensitivity can be expressed by

$$\frac{\partial f^*}{\partial x_e} = \frac{\partial f}{\partial x_e} + \lambda \frac{\partial \kappa^H}{\partial x_e} \tag{21}$$

If $\kappa^H \geq \kappa^*$, meaning the constraint is already satisfied, thus λ is set as 0; when $\kappa^H < \kappa^*$, denoting the constraint is not satisfied, thus κ^H needs to be maximized first. Therefore, before calculating the modified objective function's sensitivity, λ needs to be determined, which is calculated according to the following procedures. First, an intermediate parameter *z* is introduced for controlling λ as

$$\lambda = \frac{1-z}{z} \tag{22}$$

where z changes from a very small value $z_{\min} = 10^{-20}$ to 1, thus λ ranges from 0 to infinity. To determine the value of z in each iteration, we set two bound values of z as $z_{lower} = z_{\min}$ and $z_{upper} = 1$. The programme begins with z=1 and $\frac{\partial f^*}{\partial x_e}$ is calculated via Eq. (21). According to the ranking of the sensitivities for all elements, the design variables are updated to meet the objective volume fraction in the next iteration. Then we can estimate the bulk modulus κ^H in the next iteration, κ^H_{iter+1} , based on the variation of the design variables as

$$\kappa^H_{iter+1} = \kappa^H_{iter} + \sum \frac{d\kappa^H_{iter}}{dx_e} \Delta x_e \tag{23}$$

If $\kappa^H_{iter+1} < \kappa^*$, meaning the constraint is not satisfied, λ is then enlarged by moving the upper bound z_{upper} to z and meanwhile updating z with a smaller value

$$z = \frac{z + z_{lower}}{2} \tag{24}$$

If $\kappa^H_{iter+1} > \kappa^*$, meaning the constraint is already satisfied, the lower bound z_{upper} is moved to z and meanwhile z is updated with a larger value as

$$z = \frac{z + z_{upper}}{2} \tag{25}$$

We repeat the above procedures multiple times until $z_{upper} - z_{lower} \le 10^{-15}$ and a suitable λ is got.

Upon determining the value of λ, the modified objective function's sensitivity, $\frac{\partial f^*}{\partial x_e}$, can be calculated according to Eq. (21), based on which we update the design variables using BESO.

BESO begins with an initial design almost full of air and gradually decreases the air's volume fraction to the objective volume fraction V_f^* by

$$V_{f,iter+1}^2 = \max\left(V_{f,iter}^2(1-ER), V_f^*\right) \tag{26}$$

in which *ER* denotes the evolutionary ratio and is set as 0.01 herein. According to the relative ranking of all elements' sensitivities, the sensitivities' threshold, α_{th}^{iter}, is calculated via the bi-section method to satisfy the volume fraction of air in the next iteration, $V_{f,iter+1}^2$. BESO will increase design variable values for elements with higher sensitivity and meanwhile decrease design variable values for elements with lower sensitivity, according to

$$x_e^{iter+1} = \begin{cases} \min\left(x_e^{iter} + \Delta x, 1\right) & if \quad \alpha_e^{iter} > \alpha_{th}^{iter} \\ \max\left(x_e^{iter} - \Delta x, 0\right) & if \quad \alpha_e^{iter} < \alpha_{th}^{iter} \end{cases} \tag{27}$$

where α_e^{iter} denotes the sensitivity of element *e* in each iteration and $\Delta x = 0.1$ herein.

The whole optimization procedure is outlined as follows [50, 51, 61]:

Step 1: Chose the initial design and determine the BESO parameters.

Step 2: Perform finite element analysis and compute the objective and constraint functions based on Eqs. (8) and (13).

Step 3: Determine the target volume fraction of the air in the next iteration based on Eq. (26).

Step 4: Determine the Lagrangian multiplier based on Eqs. (22)-(25).

Step 5: Calculate modified objective function's sensitivity based on Eq. (21).

Step 6: Update design variables according to Eq. (27).

Step 7: Repeat Steps 2–6 until the objective function is maximized.

3. Results and discussions

In this section, first, we will create multiple dual-band SSTIs with customizable dual

bandgaps for hosting dual-band corner states. On that basis, a three-band SSTI with three bandgaps will be constructed for hosting three-band corner states. Thereafter, we will conduct the experiment to prove the existence of the three-band corner states.

3.1. Customized dual-band SSTIs

To create dual-band SSTIs, we first design SCs with dual-odd-order bandgaps by maximizing two specific odd-order bandgaps via inverse design. $\beta = 0.6$ and $V_f^* = 0.6$ are set in the program. The evolution history of the unit cell and the objective function is given in Appendix A. Figures 2-4(a) show three optimized SCs (named SC1, SC2 and SC3, respectively) with dual-odd-order bandgaps and their band diagrams. The air and resin epoxy are denoted by black and yellow, respectively. The SC1 has the 1st- and 5th-order bandgaps with the two relative bandgap sizes being 39.0% and 36.7%, respectively; the SC2 has the 1st- and 7th-order bandgaps with the two relative bandgap sizes being 30.0% and 21.2%, respectively; the SC3 has the 3rd- and 7th-order bandgaps with the two relative bandgap sizes being 55.6% and 29.8%, respectively. Then, we select two kinds of UCs, that is, the primitive UC (as denoted by the blue dashed boxes) and the translated UC (as denoted by the red dashed boxes) obtained by translating the primitive UC by (*a*/2, *a*/2), from the same SC to construct the SSTI. We term the primitive UCs in Figs. 2-4(a) as UC1A, UC2A and UC3A, and the corresponding translated UCs as UC1B, UC2B and UC3B, respectively. Next, we use the 2D polarization [21, 27, 62-66], $\mathbf{P} = \left(P_x, P_y\right)$, to characterize these UCs' topology properties, expressed by

$$P_l = \frac{1}{2}\left(\sum_n q_d^n \text{modulo } 2\right), \qquad \left(-1\right)^{q_d^n} = \frac{\eta_n\left(\mathrm{X}_d\right)}{\eta_n\left(\Gamma\right)} \tag{28}$$

where $d = x, y$ denotes the direction; $\eta_n\left(\mathrm{X}_x\right)$, $\eta_n\left(\mathrm{X}_y\right)$ and $\eta_n\left(\Gamma\right)$ represent the parity of the *n*th band at high symmetric points X, Y and Γ, respectively; $\sum_n q_d^n$ denotes the sum of the

q_d for all bands below the target bandgap. The parity η_n can be determined according to the eigenmode profile of the *n*th band at the corresponding high symmetric point, where *s* and *d* modes have even parity (+) while the *q* mode has odd parity(-). As the UCs are C_{4v}-symmetric, $\eta_n\left(\mathrm{X}_x\right)=\eta_n\left(\mathrm{X}_y\right)$, resulting in $P_x = P_y$. Table 1 summarizes all parities at high symmetry points for UC1A, UC2A, UC3A, UC1B, UC2B and UC3B below the second bandgaps. Taking them into Eq. (28), it can be derived that the first bandgap is nontrivial for UC1A, UC2A and UC3A, whereas it is trivial for UC1B, UC2B and UC3B; the second bandgap is trivial for UC1A, UC2A and UC3A, whereas it is nontrivial for UC1B, UC2B and UC3B. Therefore, the topology properties between UC1A and UC1B, UC2A and UC2B, and UC3A and UC3B for both the first and second bandgaps are all distinct, ensuring the emergence of topological edge states at the boundary between these primitive and translated UCs. Meanwhile, the simultaneous nonzero P_x and P_y can lead to nonzero corner charge Q_c, expressed by

$$Q_c = 4P_xP_y \tag{29}$$

Accordingly, for the first bandgap, $Q_c = 1$ for UC1A, UC2A and UC3A while $Q_c = 0$ for UC1B, UC2B and UC3B; for the second bandgap, $Q_c = 0$ for UC1A, UC2A and UC3A while $Q_c = 1$ for UC1B, UC2B and UC3B. Therefore, for both the first and second bandgaps, the different topological corner charges between UC1A and UC1B, UC2A and UC2B, and UC3A and UC3B ensure the existence of topological corner states at the 90° corner formed between them.

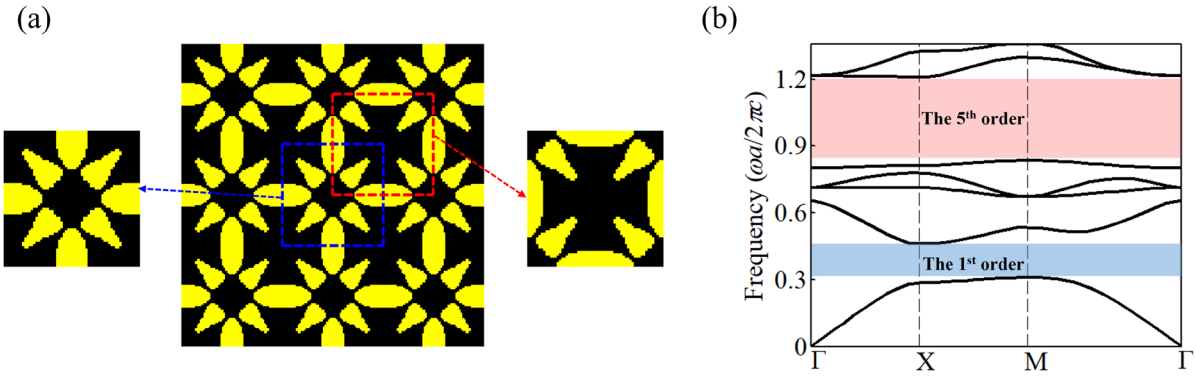

Fig. 2. The configuration of SC1 and its band diagram. (a) The optimized 3×3 unit cells. (b) The band diagram.

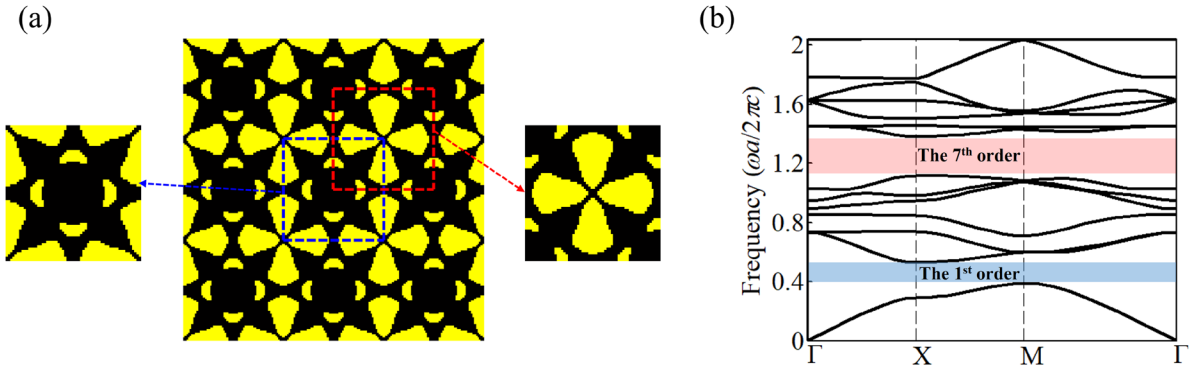

Fig. 3. The configuration of SC2 and its band diagram. (a) The optimized 3×3 unit cells. (b) The band diagram.

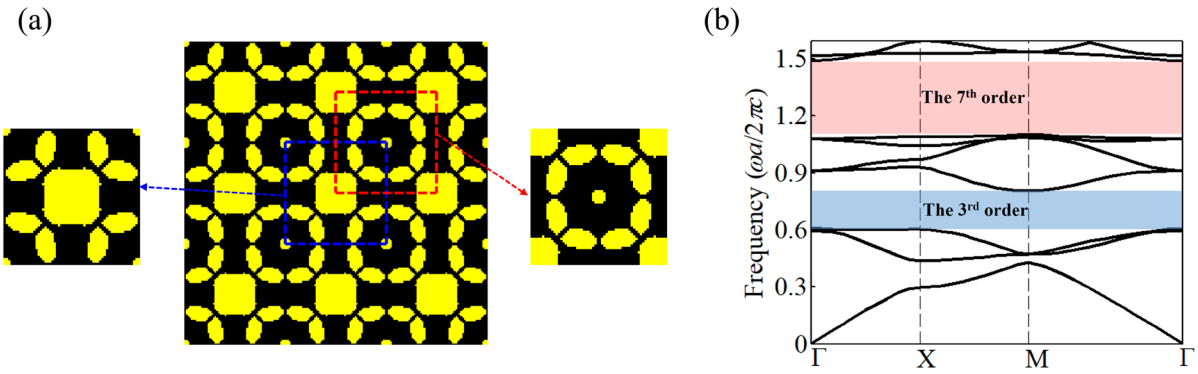

Fig. 4. The configuration of SC3 and its band diagram. (a) The optimized 3×3 unit cells. (b) The band diagram.

Table 1. Parities at high symmetry points for UC1A, UC2A, UC3A, UC1B, UC2B and UC3B

	Band order						
	1	2	3	4	5	6	7

UC1A	Γ	+	+	-	-	+		
	X	-	+	+	+	-		
UC1B	Γ	+	+	-	-	+		
	X	+	-	-	-	+		
UC2A	Γ	+	-	-	+	+	+	+
	X	-	+	+	-	-	+	-
UC2B	Γ	+	-	-	+	+	+	+
	X	+	-	-	+	+	-	+
UC3A	Γ	+	+	+	-	-	-	-
	X	+	-	+	+	-	-	-
UC3B	Γ	+	+	+	-	-	-	-
	X	-	+	-	-	+	+	+

To confirm topological edge states, we construct the supercell made of 8 UC*i*As (*i*=1, 2, 3) and 8 UC*i*Bs (*i*=1, 2, 3) with a boundary between them. The supercells made of UC1A and UC1B, UC2A and UC2B, UC3A and UC3B are termed ES1, ES2 and ES3, respectively. Figures 5(a-c) show the projected band diagrams of ES1, ES2 and ES3, respectively. It can be found that edge states appear within both the two designed bandgaps. Figures 5(d-f) demonstrate the eigenmodes of edge states in Figs. 5(a-c), showing that the energies are localized at the interfaces. To verify the corner states, we design the metastructure made of 8×8 UC*i*Bs surrounded by 4 layers of UC*i*As with a corner between them. The metastructures made of UC1A and UC1B, UC2A and UC2B, UC3A and UC3B are termed MS1, MS2 and MS3, respectively. Figures 6-8(a) give the eigenvalue spectrums for MS1, MS2, and MS3, respectively, and we can observe that corner states appear within both the two bandgaps. Figures 6-8(b) present the eigenmodes of corner states, demonstrating that the energies of these corner states are indeed localized at corners. Thus, dual-band second-order topological phases are engineered within different customized dual bandgaps. Note that we observe multiple corner states within the first bandgap of MS1 and the second bandgap of MS2 and MS3. The reason is that these structures are made of optimized unit cells with complex

configuration, which may lead to strong long-range couplings, thus resulting in multiple corner states emerging inside or outside the gapped edge states [18, 67].

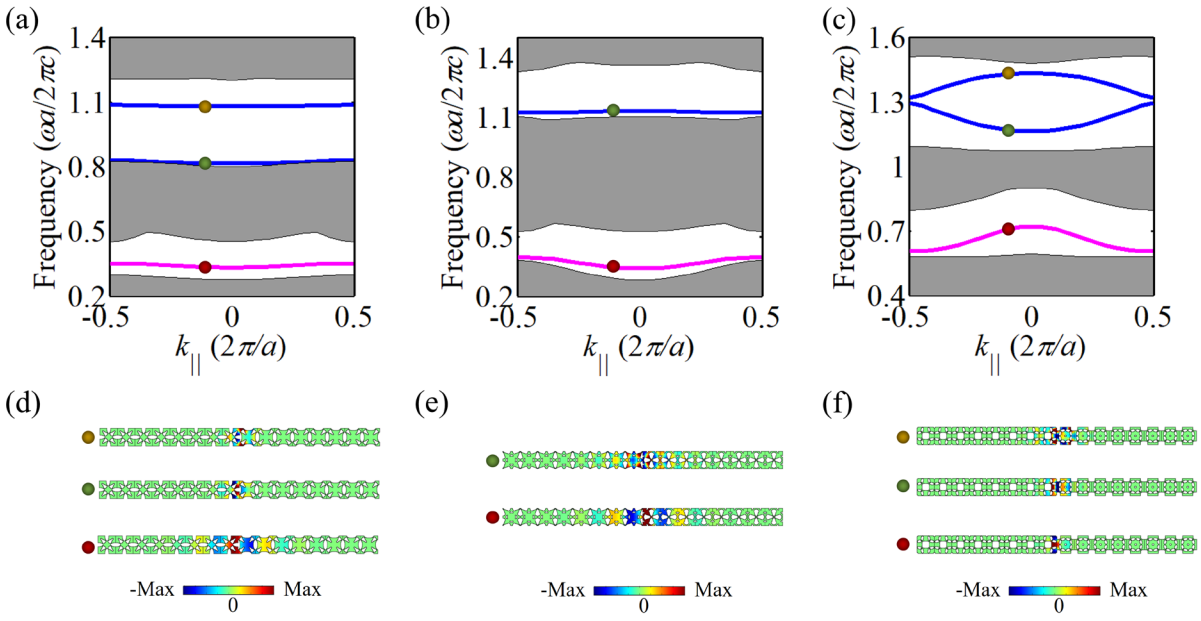

Fig. 5. (a)-(c) Projected band diagrams for ES1, ES2 and ES3, respectively. (d-f) Eigenmodes of edge states in (a-c).

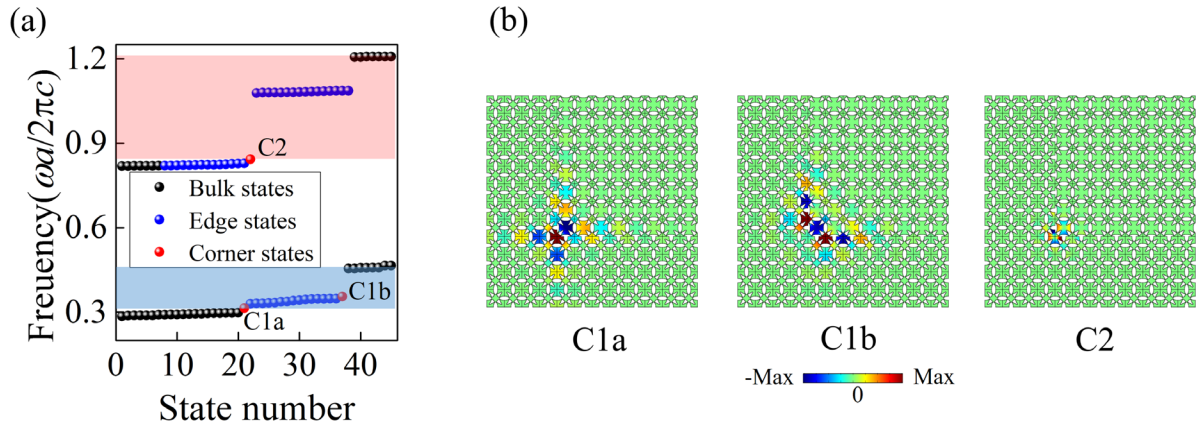

Fig. 6. (a) The eigenvalue spectrum for MS1. (b) Eigenmodes of corner states in (a).

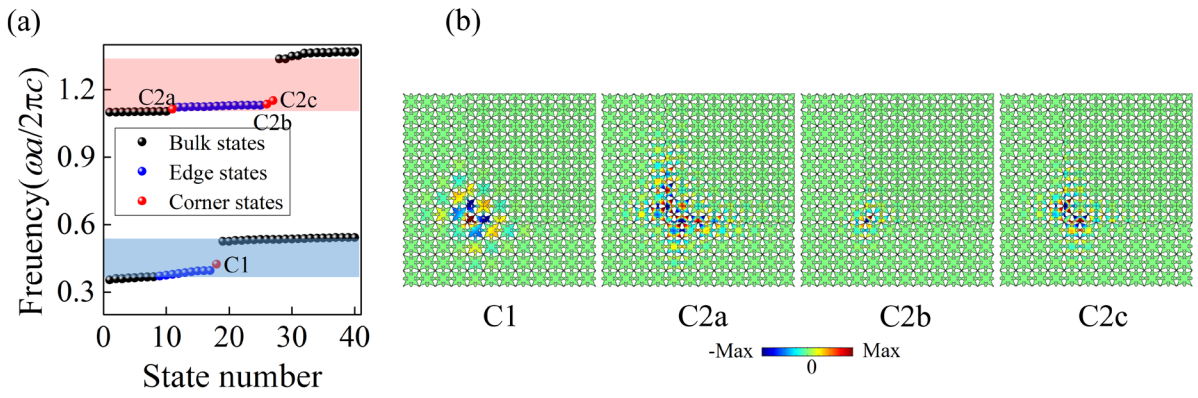

Fig. 7. (a) The eigenvalue spectrum for MS2. (b) Eigenmodes of corner states in (a).

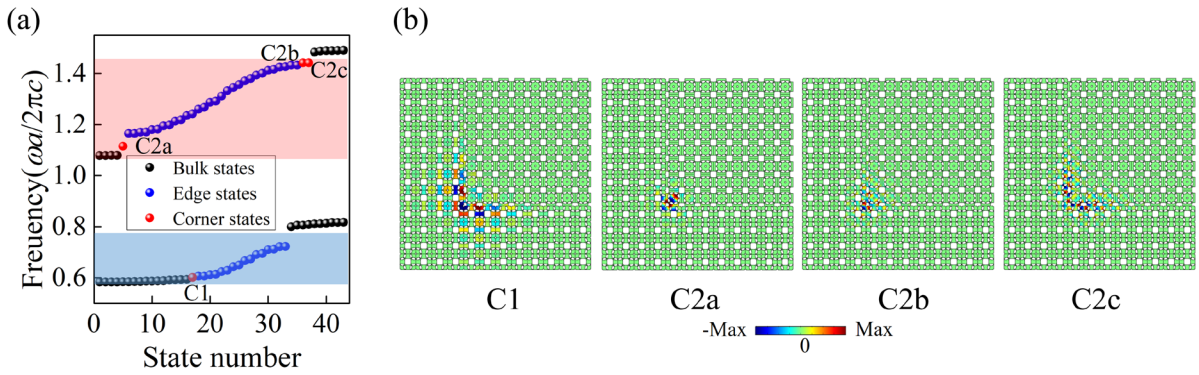

Fig. 8. (a) The eigenvalue spectrum for MS3. (b) Eigenmodes of corner states in (a).

3.2. Three-band SSTI

In this section, we maximize three odd-order bandgaps simultaneously for creating a three-band SSTI; the 1st-, 5th-, and 9th-order bandgaps are selected to be maximized. $\beta = 0.75$ and $V_f^* = 0.6$ are set in this case. Figure 9 shows the optimized SC (named SC4) and its band diagram. The relative size of 1st-, 5th-, and 9th-order bandgaps is 16.7%, 14.6% and 8.8%, respectively. Then, the primitive UC (named UC4A) and translated UC (named UC4B) are selected to construct the SSTI. Table 2 gives all high symmetry points' parities for UC4A and UC4B below the third bandgap. Taking those parities into Eq. (28), it can be derived that, for UC4A, the 1st-order band gap is nontrivial and the 5th- and 9th-order bandgaps are trivial, while for UC4B, the 1st-order bandgap is trivial and the 5th- and 9th-order bandgaps are

nontrivial. Therefore, all three bandgaps between UC4A and UC4B have distinct topology properties, offering the possibility for engineering topological phases within these bandgaps.

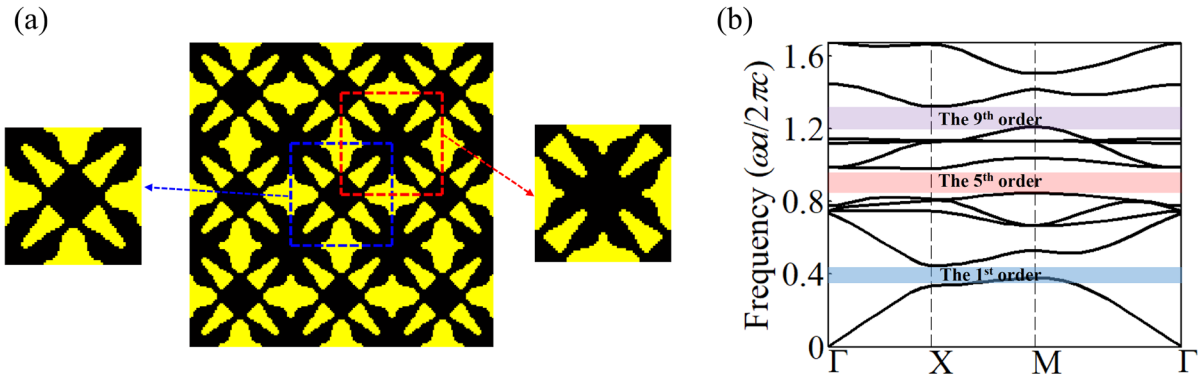

Fig. 9. The configuration of SC4 and its band diagram. (a) The optimized 3×3 unit cells. (b) The band diagram.

Table 2. Parities at high symmetry points for UC4A and UC4B

		Band order								
		1	2	3	4	5	6	7	8	9
UC7A	Γ	+	+	-	-	+	-	-	+	+
	X	-	+	+	+	-	-	+	-	+
UC7B	Γ	+	+	-	-	+	-	-	+	+
	X	+	-	-	-	+	+	-	+	-

To confirm topological edge states, the supercell (termed ES4) made of 8 UC4As and 8 UC4Bs with a boundary between them is built. Figure 10(a) shows the projected band diagram of ES4, and it can be observed that edge states emerge within all three bandgaps. Figure 10(b) demonstrates the eigenfields of edge states in Fig. 10(a), showing that the energies are highly localized at the interface. To confirm the three-band corner states, we create the metastructure (termed as MS4) made of 6×6 UC4Bs surrounded by 5 layers of UC4As with a corner between them. Figure 11(a) gives the eigenvalue spectrum for MS4, showing that corner states emerge within all three bandgaps. Figure 11(b) gives the eigenmodes of corner states, demonstrating that the energies of these corner states are indeed localized at corners.

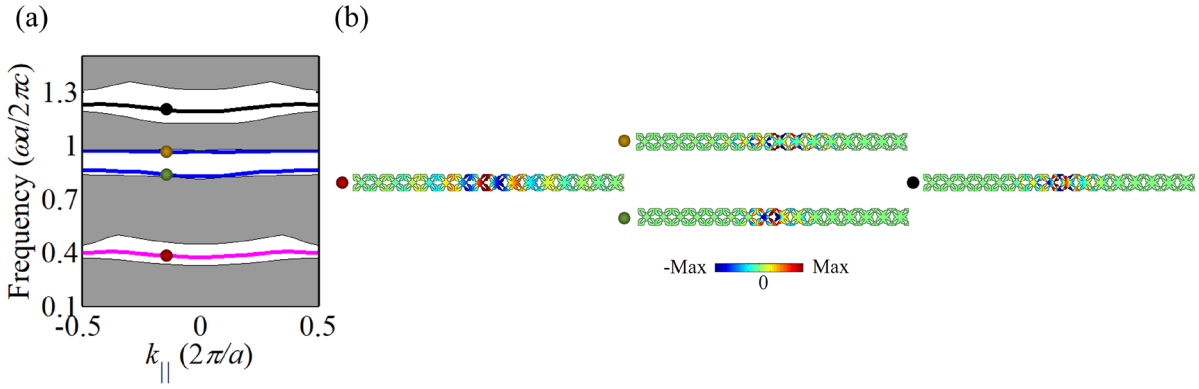

Fig. 10. (a) The projected band diagram for ES4. (b) Eigenmodes of edge states in (a).

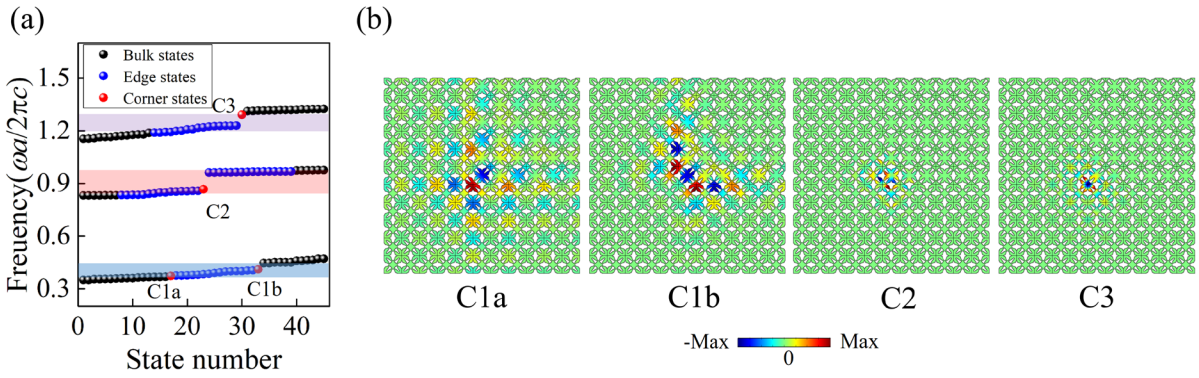

Fig. 11. (a) The eigenvalue spectrum for MS4. (b) Eigenmodes of corner states in (a).

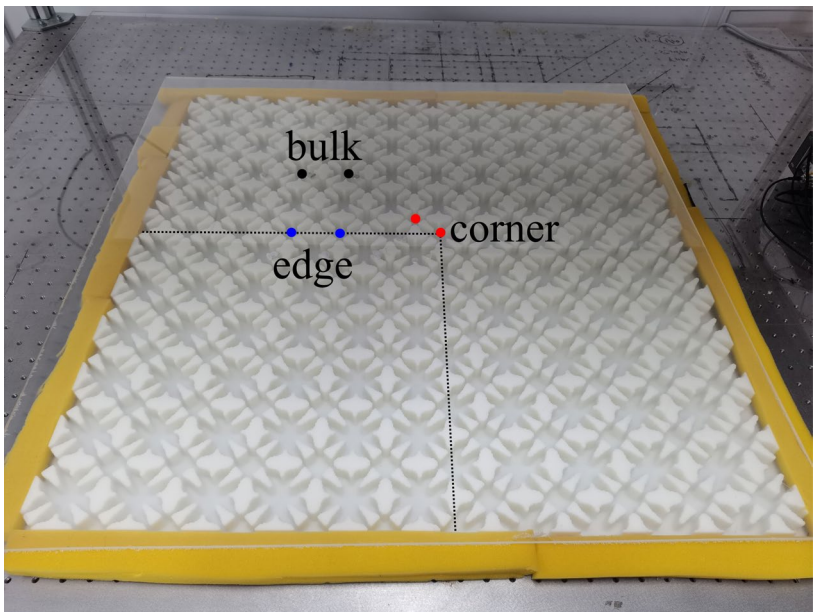

Fig. 12. The fabricated sample.

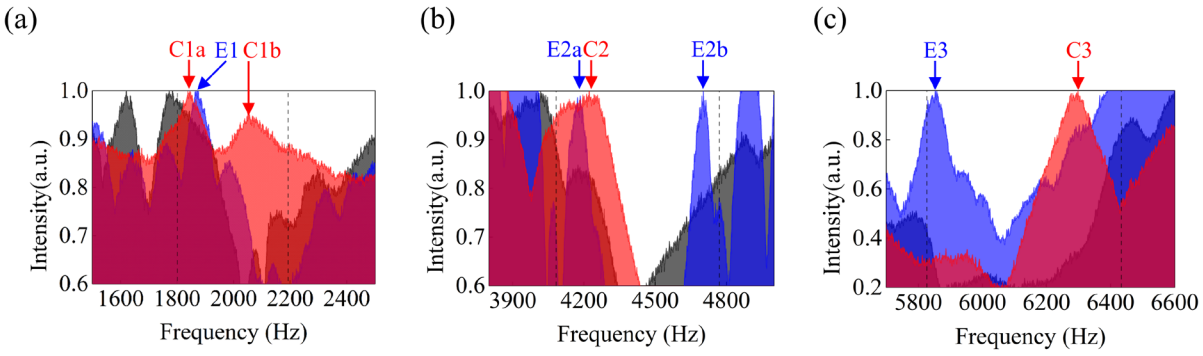

Fig. 13. Experimentally measured bulk (black), edge (blue), and corner (red) spectra around (a) the first bandgap, (b) the second bandgap and (c) the third bandgap. The frequency ranges of the bandgaps are denoted by dashed lines. The peaks of corner spectra are denoted by C1a, C1b, C2 and C3, respectively, and those of edge spectra are denoted by E1, E2a, E2b, and E3, respectively.

To experimentally validate the three-band corner states, we fabricate the MS4 via 3D printing, as shown in Fig. 12. The boundary between UC4A and UC4B is denoted by the black dashed line. The sample is made of photosensitive resin, which can be regarded as hard boundaries for sound. The lattice constant of the unit cell is 70 mm. An acrylic plate is added on the top of the sample (the height is 20 mm) to form a two-dimensional waveguide for measurement. The transparent plate is perforated with multiple holes, sealed when not in use, for inserting the acoustic source or detector. We label three pairs of holes for measuring bulk, edge, and corner spectra as black, blue, and red circles, respectively. For one pair of holes, one is used for inserting the acoustic source and the other for detector. Figures 13(a-c) show the measured bulk (black), edge (blue), and corner (red) response spectra around the three bandgaps; the numerically calculated frequency ranges of the bulk bandgaps are denoted by dashed lines. We can find that, within the three bulk bandgaps, the response spectra of bulk states have obvious dips. Meanwhile, we can observe multiple peaks of edge and corner response spectra within bulk bandgaps, indicating the existence of corner and edge states,

corresponding to the calculated spectrum in Fig. 11(a). The measured frequencies of corner states C1a, C1b, C2, and C3 are 1845 Hz, 2054 Hz, 4222Hz and 6298 Hz, respectively, while the numerically calculated frequencies of these corner states are 1828 Hz, 2016 Hz, 4253 Hz and 6331 Hz, respectively. The relative errors of frequencies of corner states C1a, C1b, C2, and C3 between experiment and numerical calculation are 0.93%, 1.9%, 0.73% and 0.52%, respectively. These tiny errors mainly come from fabrication errors and can be acceptable. Therefore, the three-band corner states are experimentally validated.

4. Conclusions

In summary, we create multiband SSTIs hosting corner states within customizable multiple bandgaps via inverse design. The inverse design is formulated to maximize customizable multiple odd-order bandgaps of SCs. Trivial and nontrivial UCs are selected from the optimized SC in distinct ways. By arranging them to form a metastructure with a corner, multiband SSTIs are constructed. We first design three dual-band SSTIs hosting corner states within customizable double bandgaps. On that basis, we create one three-band SSTI hosting corner states within three bandgaps. Thereafter, the designed three-band SSTI is fabricated and the three-band corner states are validated experimentally. The multiband SSTIs we proposed may have promising applications for robust multiband applications of sound waves.

Appendix A: Evolution history of the unit cell

Our numerical experiences show that it is difficult to maximize the multiple bandgaps simultaneously from a simple initial structure. To overcome this problem, we adopt a two-stage method in the optimization. At the first stage, we maximize the relative size of one bandgap. Then the optimized unit cell from the first stage is used as the initial structure at the second stage for maximizing the multiple bandgaps simultaneously. Here, we demonstrate

the two-stage evolution histories of the unit cell and bandgap-midgap ratio for designing the SC1 with the first-order and fifth-order bandgaps. Figure A1(a) presents the evolution history of the unit cell and the bandgap-midgap ratio at the first stage, wherein the fifth-order bandgap is maximized. It can be seen that the size of the fifth-order bandgap is gradually enlarged from the negative value, which means no bandgap, to the maximum value. In the meantime, the unit cell evolves into the optimal configuration with clear boundaries. Importantly, due to the imposed constraint, the air domains are connected into one block. Figure A1(b) shows the evolution history of the unit cell and the bandgap-midgap ratio at the second stage, wherein the optimized unit cell from the first stage is used as the initial structure and the first-order and fifth-order bandgaps are maximized simultaneously. We can find that, at initial iterations, the size of the first-order bandgap gradually increases while that of the fifth-order bandgap gradually decreases; then the sizes of first-order and fifth-order bandgaps gradually increase to the same value.

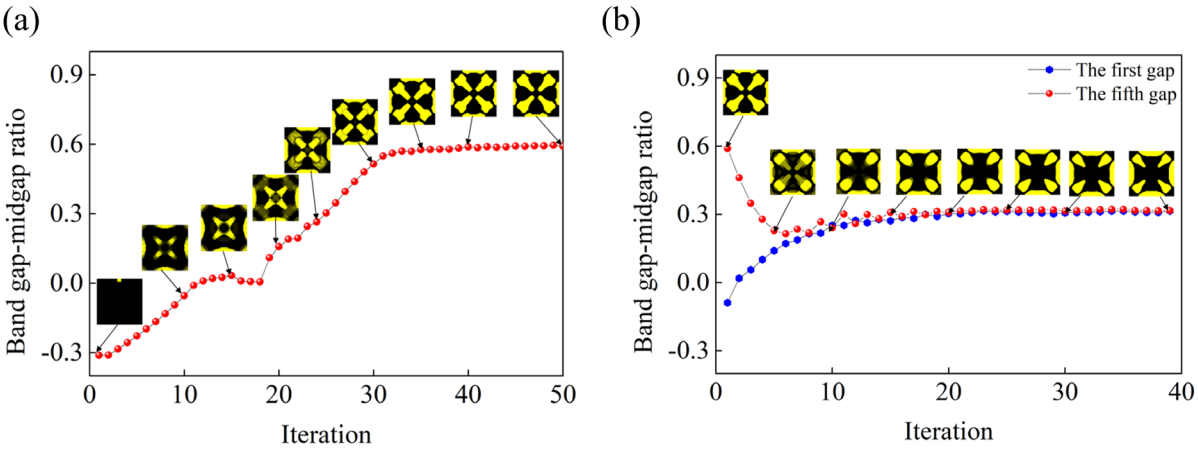

Fig. A1. The two-stage evolution histories of the unit cell and bandgap-midgap ratio for designing the SC1: (a) the first stage; (b) the second stage.

Acknowledgements

This work is supported by the National Natural Science Foundation of China (No. 1210020421), the Natural Science Foundation of Hunan Province (2022JJ40026), the

Fundamental Research Funds for the Central Universities (Grant No. 22120220237), and the Research Grants Council of Hong Kong SAR (Grant AoE/P-502/20, 15205219, 15202820 and 15204419). Yafeng Chen would like to thank Dr. Fei Meng in Wuhan University of Technology for discussing bandgap optimization method.

References

[1] G. Ma, M. Xiao, C.T. Chan, Topological phases in acoustic and mechanical systems, Nature Reviews Physics 1(4) (2019) 281-294.
[2] H. Xue, Y. Yang, B. Zhang, Topological acoustics, Nature Reviews Materials (2022) 1-17.
[3] X. Zhang, M. Xiao, Y. Cheng, M.-H. Lu, J. Christensen, Topological sound, Communications Physics 1(1) (2018) 97.
[4] Z. Gu, H. Gao, P.-C. Cao, T. Liu, X.-F. Zhu, J. Zhu, Controlling sound in non-hermitian acoustic systems, Physical Review Applied 16(5) (2021) 057001.
[5] Z. Gu, H. Gao, T. Liu, S. Liang, S. An, Y. Li, J. Zhu, Topologically protected exceptional point with local non-hermitian modulation in an acoustic crystal, Physical Review Applied 15(1) (2021) 014025.
[6] H. Fan, H. Gao, T. Liu, S. An, X. Kong, G. Xu, J. Zhu, C.-W. Qiu, Z. Su, Reconfigurable topological modes in acoustic non-Hermitian crystals, Physical Review B 107(20) (2023) L201108.
[7] Z. Gu, H. Gao, H. Xue, J. Li, Z. Su, J. Zhu, Transient non-Hermitian skin effect, Nature Communications 13(1) (2022) 7668.
[8] H. Gao, H. Xue, Z. Gu, L. Li, W. Zhu, Z. Su, J. Zhu, B. Zhang, Y. Chong, Anomalous Floquet non-Hermitian skin effect in a ring resonator lattice, Physical Review B 106(13) (2022) 134112.
[9] H.-X. Wang, Z.-K. Lin, B. Jiang, G.-Y. Guo, J.-H. Jiang, Higher-order Weyl semimetals, Physical Review Letters 125(14) (2020) 146401.
[10] Z. Yang, F. Gao, X. Shi, X. Lin, Z. Gao, Y. Chong, B. Zhang, Topological acoustics, Physical review letters 114(11) (2015) 114301.
[11] C. He, X. Ni, H. Ge, X.-C. Sun, Y.-B. Chen, M.-H. Lu, X.-P. Liu, Y.-F. Chen, Acoustic topological insulator and robust one-way sound transport, Nature Physics 12(12) (2016) 1124.
[12] J. Lu, C. Qiu, L. Ye, X. Fan, M. Ke, F. Zhang, Z. Liu, Observation of topological valley transport of sound in sonic crystals, Nature Physics 13(4) (2017) 369.
[13] B. Xia, H. Fan, T. Liu, Topologically protected edge states of phoxonic crystals, International Journal of Mechanical Sciences 155 (2019) 197-205.
[14] Y.-G. Peng, C.-Z. Qin, D.-G. Zhao, Y.-X. Shen, X.-Y. Xu, M. Bao, H. Jia, X.-F. Zhu, Experimental demonstration of anomalous Floquet topological insulator for sound, Nature communications 7 (2016) 13368.
[15] H. Xue, Y. Yang, F. Gao, Y. Chong, B. Zhang, Acoustic higher-order topological insulator on a kagome lattice, Nature materials 18(2) (2019) 108-112.
[16] X. Zhang, H.-X. Wang, Z.-K. Lin, Y. Tian, B. Xie, M.-H. Lu, Y.-F. Chen, J.-H. Jiang, Second-order topology and multidimensional topological transitions in sonic crystals, Nature Physics 15(6) (2019) 582-588.
[17] H. Gao, H. Xue, Z. Gu, T. Liu, J. Zhu, B. Zhang, Non-Hermitian route to higher-order topology in an acoustic crystal, Nature communications 12(1) (2021) 1-7.
[18] S. An, T. Liu, H. Fan, H. Gao, Z. Gu, S. Liang, S. Huang, Y. Zheng, Y. Chen, L. Cheng, Second-order elastic topological insulator with valley-selective corner states, International

Journal of Mechanical Sciences 224 (2022) 107337.
[19] L. Yang, Y. Wu, K. Yu, R. Zhao, W. Wang, B. Bonello, B. Djafari-Rouhani, Robust Fano resonance between mechanical first-and second-order topological states, International Journal of Mechanical Sciences 236 (2022) 107768.
[20] X. Zhang, B.-Y. Xie, H.-F. Wang, X. Xu, Y. Tian, J.-H. Jiang, M.-H. Lu, Y.-F. Chen, Dimensional hierarchy of higher-order topology in three-dimensional sonic crystals, Nature communications 10(1) (2019) 1-10.
[21] Z. Zhang, M.R. López, Y. Cheng, X. Liu, J. Christensen, Non-Hermitian sonic second-order topological insulator, Physical review letters 122(19) (2019) 195501.
[22] X. Zhang, L. Liu, M.-H. Lu, Y.-F. Chen, Valley-Selective Topological Corner States in Sonic Crystals, Physical Review Letters 126(15) (2021) 156401.
[23] Z. Zhang, B. Hu, F. Liu, Y. Cheng, X. Liu, J. Christensen, Pseudospin induced topological corner state at intersecting sonic lattices, Physical Review B 101(22) (2020) 220102.
[24] X. Zhang, Z.-K. Lin, H.-X. Wang, Z. Xiong, Y. Tian, M.-H. Lu, Y.-F. Chen, J.-H. Jiang, Symmetry-protected hierarchy of anomalous multipole topological band gaps in nonsymmorphic metacrystals, Nature communications 11(1) (2020) 1-9.
[25] L. Luo, H.-X. Wang, Z.-K. Lin, B. Jiang, Y. Wu, F. Li, J.-H. Jiang, Observation of a phononic higher-order Weyl semimetal, Nature Materials 20(6) (2021) 794-799.
[26] J. Ma, X. Xi, X. Sun, Experimental Demonstration of Dual-Band Nano-Electromechanical Valley-Hall Topological Metamaterials, Advanced Materials (2021) 2006521.
[27] L. Fan, Y. Chen, S. An, T. Liu, H. Fan, J. Zhu, Z. Su, Local-Resonance-Induced Dual-Band Topological Corner States of Flexural Waves in a Perforated Metaplate, Physical Review Applied 19(3) (2023) 034065.
[28] Y. Chen, Z. Lan, Z. Su, J. Zhu, Inverse design of photonic and phononic topological insulators: a review, Nanophotonics 11(19) (2022) 4347-4362.
[29] Y. Chen, F. Meng, X. Huang, Creating acoustic topological insulators through topology optimization, Mechanical Systems and Signal Processing 146 (2021) 107054.
[30] Y. Chen, F. Meng, B. Jia, G. Li, X. Huang, Inverse Design of Photonic Topological Insulators with Extra-Wide Bandgaps, Physica Status Solidi-Rapid Research Letters 13(9) (2019) 1900175
[31] Y. Chen, D. Chen, B. Liu, Topology Optimization of Phononic Dirac-Like Cones and Topological Insulators with On-Demand Operation Frequencies, Advanced Theory and Simulations (2022) 2200103.
[32] R.E. Christiansen, F. Wang, O. Sigmund, S. Stobbe, Designing photonic topological insulators with quantum-spin-Hall edge states using topology optimization, Nanophotonics 8(8) (2019) 1363-1369.
[33] R.E. Christiansen, F. Wang, O. Sigmund, Topological insulators by topology optimization, Physical Review Letters 122(23) (2019) 234502.
[34] Y. Lu, H.S. Park, Double Dirac cones and topologically nontrivial phonons for continuous square symmetric C 4 (v) and C 2 (v) unit cells, Physical Review B 103(6) (2021) 064308.
[35] J. Luo, Z. Du, C. Liu, Y. Mei, W. Zhang, X. Guo, Moving Morphable Components-based inverse design formulation for quantum valley/spin hall insulators, Extreme Mechanics Letters 45 (2021) 101276.
[36] Z. Du, H. Chen, G. Huang, Optimal quantum valley Hall insulators by rationally engineering Berry curvature and band structure, Journal of the Mechanics and Physics of Solids 135 (2020) 103784.
[37] J. Zhang, F. Wang, O. Sigmund, L. Gao, R.E. Christiansen, Ultra-broadband edge-state

pair for zigzag-interfaced valley Hall insulators, Science China Physics, Mechanics & Astronomy 65(5) (2022) 1-9.
[38] Y. Chen, F. Meng, Z. Lan, B. Jia, X. Huang, Dual-Polarization Second-Order Photonic Topological Insulators, Physical Review Applied 15(3) (2021) 034053.
[39] Y. Chen, F. Meng, Y. Kivshar, B. Jia, X. Huang, Inverse design of higher-order photonic topological insulators, Physical Review Research 2(2) (2020) 023115.
[40] Y. Chen, F. Meng, J. Zhu, X. Huang, Inverse design of second-order photonic topological insulators in C3-symmetric lattices, Applied Mathematical Modelling 102 (2022) 194-206.
[41] Y. Chen, Z. Lan, J. Zhu, Inversely Designed Second-Order Photonic Topological Insulator With Multiband Corner States, Physical Review Applied 17(5) (2022) 054003.
[42] Y. Chen, J. Li, J. Zhu, Topology optimization of quantum spin Hall effect-based second-order phononic topological insulator, Mechanical Systems and Signal Processing 164 (2022) 108243.
[43] Z. Du, J. Luo, Z. Xu, Z. Jiang, X. Ding, T. Cui, X. Guo, Higher-order topological insulators by ml-enhanced topology optimization, International Journal of Mechanical Sciences 255 (2023) 108441.
[44] Z. Zheng, J. Yin, J. Wen, D. Yu, X. Chen, Switchable corner states in phononic crystals realized by inverse design, International Journal of Mechanical Sciences 243 (2023) 108035.
[45] Y. Chen, On the use of topology optimized band gap structures for the realization of second-order acoustic topological insulators with valley-selective corner states, Structural and Multidisciplinary Optimization 65(4) (2022) 1-11.
[46] Y. Chen, Z. Lan, J. Zhu, Second-order topological phases in C 4v -symmetric photonic crystals beyond the two-dimensional Su-Schrieffer–Heeger model, Nanophotonics (2022).
[47] Y. Chen, Z. Lan, J. Li, J. Zhu, Topologically protected second harmonic generation via doubly resonant high-order photonic modes, Physical Review B 104(15) (2021) 155421.
[48] V. Laude, Phononic Crystals: Artificial Crystals for Sonic, Acoustic, and Elastic Waves, Walter de Gruyter GmbH & Co KG2015.
[49] C. Kittel, Introduction to solid state physics : 6th ed, American Journal of Physics 61(1) (2011) 59.
[50] F. Meng, X. Huang, B. Jia, Bi-directional evolutionary optimization for photonic band gap structures, Journal of Computational Physics 302 (2015) 393-404.
[51] Y.F. Li, X. Huang, F. Meng, S. Zhou, Evolutionary topological design for phononic band gap crystals, Structural and Multidisciplinary Optimization (2016) 1-23.
[52] Y. Li, Y. Luo, X. Zhang, Topological design of phononic crystals for multiple wide band gaps, Journal of Sound and Vibration 529 (2022) 116962.
[53] Y. Chen, F. Meng, G. Sun, G. Li, X. Huang, Topological design of phononic crystals for unidirectional acoustic transmission, Journal of Sound Vibration 410 (2017) 102-123.
[54] O. Sigmund, Tailoring materials with prescribed elastic properties, Mechanics of Materials 20(4) (1995) 351-368.
[55] M.P. Bendsøe, N. Kikuchi, Generating optimal topologies in structural design using a homogenization method, Computer methods in applied mechanics and engineering 71(2) (1988) 197-224.
[56] Z. Hashin, S. Shtrikman, A variational approach to the theory of the elastic behaviour of multiphase materials, Journal of the Mechanics and Physics of Solids 11(2) (1963) 127-140.
[57] X. Huang, Y. Xie, Evolutionary topology optimization of continuum structures: methods and applications, John Wiley & Sons2010.
[58] V. Komkov, K.K. Choi, E.J. Haug, Design sensitivity analysis of structural systems, Academic press1986.
[59] Y.F. Li, X. Huang, S. Zhou, Topological design of cellular phononic band gap crystals,

Materials 9(3) (2016) 186.
[60] Y. Chen, D. Guo, Y.F. Li, G. Li, X. Huang, Maximizing wave attenuation in viscoelastic phononic crystals by topology optimization, Ultrasonics 94 (2019) 419-429.
[61] Y. Li, X. Huang, S. Zhou, Topological design of cellular phononic band gap crystals, Materials 9(3) (2016) 186.
[62] F. Liu, H.-Y. Deng, K. Wakabayashi, Helical Topological Edge States in a Quadrupole Phase, Physical Review Letters 122(8) (2019) 086804.
[63] Z. Zhang, H. Long, C. Liu, C. Shao, Y. Cheng, X. Liu, J. Christensen, Deep-Subwavelength Holey Acoustic Second-Order Topological Insulators, Advanced Materials 31(49) (2019) 1904682.
[64] W.A. Benalcazar, T. Li, T.L. Hughes, Quantization of fractional corner charge in C n-symmetric higher-order topological crystalline insulators, Physical Review B 99(24) (2019) 245151.
[65] Y. Chen, J. Zhu, Z. Su, Topology optimization of a second-order phononic topological insulator with dual-band corner states, Journal of Sound and Vibration 544 (2023) 117410.
[66] Y. Chen, Z. Lan, J. Zhu, Z. Su, Creating anisotropic topological phases within inversely designed photonic crystals, Optics & Laser Technology 158 (2023) 108865.
[67] Y. Chen, X. Lu, H. Chen, Effect of truncation on photonic corner states in a Kagome lattice, Optics letters 44(17) (2019) 4251-4254.